INSTABILITY OF THE FLOW IN ROTATING CAVITY

Ewa Tuliszka-Sznitko
Artur Zieliński

Technical University of Poznań , Institute of Thermal Engineering, Poland

e-mail: sznitko@sol.put.poznan.pl

The transitional flow in rotating cavity is investigated numerically by Direct Numerical Simulation (DNS), Large Eddy Simulation (LES) and theoretical (LSA) methods. LSA results coupled with accurate numerical DNS and LES computations based on an efficient pseudo-spectral Chebyshev-Fourier method, brings new insight into the spatio-temporal characteristics of the isothermal and not-isothermal flows in the rotating cavities. DNS and LES computations have been performed for a wide range of Reynolds numbers to analyze different stages of the transition process. Computations have been performed for different geometrical configurations, including co- and counter-rotating cavities with through-flow.

Key words: laminar-turbulent transition, rotating cavity, direct method

1. Introduction

The flow in rotating disks system is not only a subject of fundamental interest but it is also a topic of practical importance. Typical configurations are cavities between the rotating compressors and turbines' disks. Numerous works have been recently devoted to investigation of the instabilities, associated with a single disk flow and with a differently rotating disks flow, cf. Serre *et al.* (2001a,b, 2004), Lingwood (1997), Tuliszka-Sznitko and Soong (2000), Tuliszka-Sznitko *et al.* (2002), Itoh (1991). For the high rotation rate, the flow in a rotor/stator cavity consists of two boundary layers, of the Ekman type on the rotating disk and of the Bödewadt type on the stationary disk, separated by an inviscid rotating core. The transition process in both layers is related to the type I and type II generic linear instabilities. Type I instability is the inviscid instability. The mechanism of type II instability is related to the combined effects of the Coriolis and viscous forces. The instability structures in the rotor/stator cavity were investigated numerically and experimentally

among others by Dijkstra and van Heijst (1983), Serre *et al.* (2001a, 2004), Gauthier *et al.* (2002), Schouveiler *et al.* (1999, 2001). The stability of co- and counter-rotating disks' cavity was studied by Gauthier *et al.* (2002) and Moisy *et al.* (2004).

Non-isothermal flow conditions were also considered (Mochizuki and Yang Wen-Jei, 1986; Tuliszka-Sznitko and Soong, 2000; Tuliszka-Sznitko and Zieliński, 2006a), showing that the thermal effects and the rotation-induced buoyancy become influential on the stability characteristics and on the critical conditions. The most interesting from point of view of applications are cases with a superimposed radial outflow of cooling air, which are often used to remove heat from co-rotating turbine discs. Many experimental and numerical investigations have been conducted in an attempt to understand this kind of flows and to use expensive cooling air more effectively (Bohn *et al.*, 1994; Owen and Rogers, 1995; Chew *et al.*, 1984).

DNS method is mostly used to investigate transitional flow between rotating disks by solving 3D Navier Stokes, continuity and, in the case of not-isothermal flow, energy equations. With DNS all relevant length-scales and time-scales of motion are resolved. However, the required computational recourses are large because CPU time increases as Re_R^3. Due to the CPU time requirements, computations are limited to flows of low or moderate Reynolds number. It means that only transitional or weakly turbulent flow is computed by DNS. For high Reynolds number the RANS method is commonly used in which only the mean flow is computed by solving Reynolds – averaged Navier-Stokes equations and the effect of turbulence on the mean flow is modeled. The computational cost is small in comparison with the cost of DNS, however capability of the method is limited. The existing models of turbulence, mostly using the isotropy assumption, are not sufficient for numerical investigations of the rotating flows. Large Eddy Simulation (LES) is an intermediate approach in which the effect of large scales is directly computed and only the small subgrid scales are modeled. Since small scales are more isotropic than the large ones, it should be possible to parameterize them using simpler and more universal models than the RANS models.

In the paper, we present our theoretical and numerical investigations on the transitional isothermal and non-isothermal flows in rotating cavity. Our early LSA computations were used to enlighten the DNS and LES results with respect to type I and II instabilities. Moreover, the absolute instability regions which are supposed to be strongly connected with the turbulent breakdown process were identified by the LSA method. The three-dimensional DNS and LES computations have been performed for an annular roror/rotor cavity of aspect ratio $L = 9$ and curvature parameters $R_m = 1.5$, 3.0. DNS results obtained for the cylindrical cavity of aspect ratio $L = 5$ (published in Serre *et al.*, 2004) are also discussed.

For the not-isothermal flow the Boussinesq approximation was used. Non-isothermal computations allowed us to analyze the influence of the thermal Rossby number on the instability structures and on critical parameters. The distributions of the local Nusselt numbers along the radius of the disks are presented. The isothermal and non-isothermal flows with a superimposed radial outflow of cooling air are analyzed.

In the present paper the geometrical and mathematical models are presented in Section 2. The LSA, DNS and LES numerical solution techniques are described in Section 3. In Sections 4 and 5 the obtained results are analyzed. In Section 6 concluding remarks are given.

2. Geometrical and mathematical model

The geometrical model is a cavity between co- and counter-rotating disks with and without throughflow (Fig. 1). The cavity, bounded by an outer cylinder of radius R_1^* and height $2h$ is called cylindrical and the cavity bounded by inner and outer cylinders of radiuses R_0^* and R_1^* is called annular. The faster rotating disk rotates at uniform angular velocity $\boldsymbol{\Omega}_1^* = \Omega_1^* \boldsymbol{e}_z$, $\boldsymbol{e}_z$ being the unit vector. The slower rotating disk rotates at angular velocity $\Omega_2^* = s\Omega_1^*$. Positive s means that both disks rotate in the same direction and negative s means that disks rotate in opposite directions. The flow is controlled by the following physical parameters: the Reynolds number based on the external radius of the disks and on the angular velocity of the faster rotating disk Ω_1^*, $\mathrm{Re}_R = R_1^{*2}\Omega_1^*/\nu^*$, the local Reynolds number $\mathrm{Re}_\delta = r^*/\delta = \sqrt{r^{*2}\Omega_1^*/\nu^*}$, the aspect ratio $L = (R_1^* - R_0^*)/2h$ and the curvature parameter $R_m = (R_1^* + R_0^*)/(R_1^* - R_0^*)$. In the case of similarity solution considered in Section 3, radiuses of the disks are infinite ($L \to \infty$, $R_m = 1$). The temperatures of the upper and lower disk are denoted by T_1^* and T_2^*, respectively.
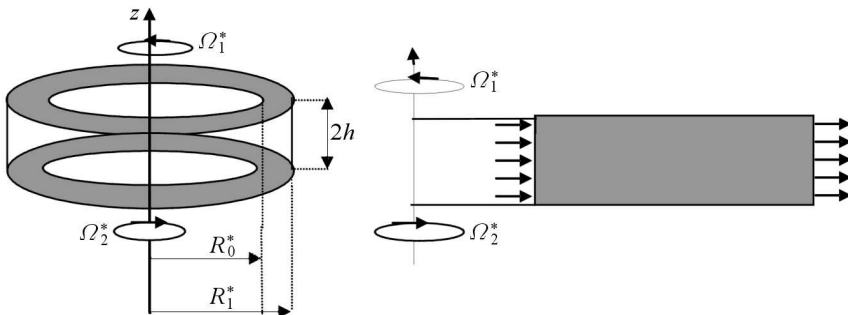

Fig. 1. Schematic picture of a rotating cavity

The flow is described by the continuity, Navier-Stokes and energy equations. The governing equations are written in a cylindrical polar coordinate system (r^*, z^*, φ), with respect to the rotating frame of reference (it is appropriate for explicit presentation of the Coriolis and centrifugal forces)

$$\nabla \cdot \boldsymbol{V}^* = 0$$
$$\rho^* \frac{\partial \boldsymbol{V}^*}{\partial t^*} + \rho^*(\boldsymbol{V}^* \cdot \nabla)\boldsymbol{V}^* + \rho^* \boldsymbol{\Omega}_1^* \times (\boldsymbol{\Omega}_1^* \times r^*) + 2\rho^* \boldsymbol{\Omega}_1^* \times \boldsymbol{V}^* =$$
$$= -\nabla p^* + \mu^* \Delta \boldsymbol{V}^* \qquad (2.1)$$
$$\frac{\partial T^*}{\partial t^*} + (\boldsymbol{V}^* \cdot \nabla)T^* = a^* \Delta T^*$$

where: t^* is time, T^* is temperature, p^* is pressure, $\boldsymbol{V}^*$ is the velocity vector, a^* is the thermal diffusivity. The time, space and velocity are normalized as follows: $(\Omega_1^*)^{-1}$, h and $\Omega_1^* R_1^*$. The dimensionless axial co-ordinate is $z = z^*/h$, $z \in [-1, 1]$. The radial coordinate is normalized additionally to obtain the domain $[-1, 1]$ requested by the spectral method based on the Chebyshev polynomials $r = (r^*/Lh - R_m)$. The dimensionless component of velocity in radial, azimuthal and axial directions are u, v and w, respectively. The dimensionless temperature is defined as $\Theta = (T^* - T_1^*)/(T_2^* - T_1^*)$. To take into account the buoyancy effects induced by the involved body forces the Boussinesq approximation is used. No slip boundary condition is applied to all rigid walls, so $u = w = 0$. For the azimuthal velocity component, the boundary conditions are $v = (R_m + r)/(R_m + 1)$ on the top of the faster rotating disk, and $v = s(R_m + r)/(R_m + 1)$ on the slower rotating disk.

3. Numerical methods

3.1. Linear stability theory

In LSA method the flow parameters are decomposed into the stationary basic state and non-stationary disturbance field. A similarity model of thermal flow with assumption of the Boussinesq fluid was formulated for generating basic solutions of axially symmetric flows (Tuliszka-Sznitko and Soong, 2000). In LSA we assume that the perturbation quantities have the following normal-mode form

$$[u', v', w', p', \tau']^\top = [\widehat{u}, \widehat{v}, \widehat{w}, \widehat{p}, \widehat{\tau}]^\top \exp(\alpha^* r^* + m\varphi - \omega^* t^*) + cc \qquad (3.1)$$

where $\widehat{u}$, $\widehat{w}$, $\widehat{v}$, $\widehat{p}$, $\widehat{\tau}$ are the dimensional amplitudes of the three components of velocity (in r^*, φ, z^* directions), pressure and temperature, respective-

ly, α^* and $\beta^* = m/r^*$ are the components of wave number k^* in the radial and azimuthal directions, respectively, m is the number of spiral vortices, ω^* is the frequency and t^* is time. Asterisk denotes dimensional values. The co-ordinate system is located on the disk under consideration. The linear stability analysis equations plus the homogeneous boundary conditions ($\widehat{u}(z^*) = \widehat{v}(z^*) = \widehat{w}(z^*) = \widehat{\tau}(z^*) = 0$ at $z^* = 0$ and $z^* = 2h$) constitute an eigenvalue problem which is solved in a global manner (Tuliszka-Sznitko and Soong, 2000).

3.2. Direct numerical simulation

In the DNS method, the numerical solution is based on a pseudo-spectral collocation Chebyshev-Fourier-Galerkin approximation. The approximation of the flow variables $\Psi = (u, w, v, p, \Theta)$ is given by a development in truncated series (Serre $et\ al.$, 2001a)

$$\Psi_{NMK}(r,z,\varphi,t) = \sum_{p=-K/2}^{K/2-1} \sum_{n=0}^{N} \sum_{m=0}^{M} \widehat{\Psi}_{nmp}(t) T_n(r) T_m(z) \mathrm{e}^{\mathrm{i}p\varphi} \qquad \begin{array}{l} -1 \leqslant r \\ z \leqslant 1 \\ 0 \leqslant \varphi \leqslant 2\pi \end{array} \tag{3.2}$$

where N, M and K are the numbers of collocation points in the radial, axial and azimuthal directions, respectively. $T_n(r)$ and $T_m(z)$ are the Chebyshev polynomials. The time scheme is semi-implicit and second-order accurate. It corresponds to a combination of the second-order backward differentiation formula for the viscous diffusion terms and the Adams-Bashforth scheme for the non-linear terms. The method uses a projection scheme to maintain the incompressibility constraint. In the case of cylindrical cavity, the singularity introduced by the axis at $r^* = 0$, requires a dependent variable transformation $\widetilde{V}^* = r^*V^*$, $\widetilde{p}^* = r^*p^*$, as proposed by Serre $et\ al.$ (2001a).

3.3. Large eddy simulation

We used the dynamic model for large eddy simulation to optimize the subgrid-scale mode coefficient. This method is used in conjunction with a new version of the dynamic Smagorinski eddy viscosity model proposed by Meneveau $et\ al.$ (1996). In this version, called a Lagrangian subgrid-scale model, the Germano $et\ al.$ (1991) identity was averaged for some time along fluid pathlines. In our incompressible computations we proceeded as follows: the filtering operation was performed only in azimuthal direction using the Gaussian function. Coefficient field is computed from the following equation (Meneveau $et\ al.$, 1996)

$$C_S^2 = \frac{L_{LM}}{L_{MM}} \tag{3.3}$$

where

$$L_{LM}^{n+1}(x) = H\{\varepsilon[L_{ij}M_{ij}]^{n+1}(x) + (1-\varepsilon)L_{LM}^n(x - \overline{u}^n \Delta t)\}$$
$$L_{MM}^{n+1}(x) = \varepsilon[M_{ij}M_{ij}]^{n+1}(x) + (1-\varepsilon)L_{MM}^n(x - \overline{u}^n \Delta t) \qquad (3.4)$$
$$\varepsilon = \frac{\Delta t/T^n}{1 + \Delta t/T^n}$$

and where x is the position along the pathline, Δt is a period of time over which averaging is performed, n and $n+1$ mean two consecutive time sections, $\overline{u}$ is an averaged velocity along the fluid-particle trajectory, $H(x)$ is the ramp function $(H(x) = x$ if $x > 0$, $H(x) = 0$ if $x < 0)$. T is the relaxation time scale, which controls the memory of the Lagrangean averaging. Some possible choices for T were given by Meneveau *et al.* (1996). In our computations we define T as follows

$$T^n = \frac{3}{2}\Delta(M_{ij}^n M_{ij}^n)^{-\frac{1}{4}} \qquad (3.5)$$

The finally obtained field of C_S is averaged in azimuthal direction.

4.   Linear stability theory results

LSA computations were performed for the co- and counter-rotating disks and for the thermal Rosby number from -0.1 to 0.1 (Tuliszka-Sznitko and Soong, 2000). For the rotor/stator case the flow consists of two disjoined boundary layers on both disks, separated by an inviscid core which rotates as a solid body. As in Itoh (1991), the solid-body angular velocity is constant and equal to $v^*/\Omega_1^* r^* = -0.687$ in the rotating frame of reference. In order to take into account the buoyancy effects, the Boussinesq approximation is invoked. In the case of non-isothermal flow, the influence of the thermal effects and the rotational-induced buoyancy on stability characteristics and the critical conditions becomes important. We have found two types of instability in both boundary layers: type II and type I. In the Bödewadt layer on the stationary disk, the onset of the type II instability has been found at $\mathrm{Re}_{\delta cII} = 34.7$. The type II instability exists only in a narrow range of Re_δ, disappearing at $\mathrm{Re}_\delta = 68$. The type I instability occurs at a slightly larger Reynolds number, $\mathrm{Re}_{\delta cI} = 47.5$. The exemplary iso-lines of the temporal amplification rate ω_i obtained at different local Reynolds numbers $\mathrm{Re}_\delta = 65$, 80 and 130 are shown in the plane of the wave-angle and wave-number (ε, k) in Fig. 2. Our results show that the Ekman layer on the rotating disk is much more stable than the Bödewadt layer with respect to type I and type II instabilities. The onset of type II instability has been found at $\mathrm{Re}_{\delta cII} = 90.23$ and type I at

$\mathrm{Re}_{\delta cI} = 278.6$. Our isothermal linear stability results of the Bödewadt and Ekman layers characterizing the type I and type II instabilities are in very good accordance with the results of Itoh (1991).
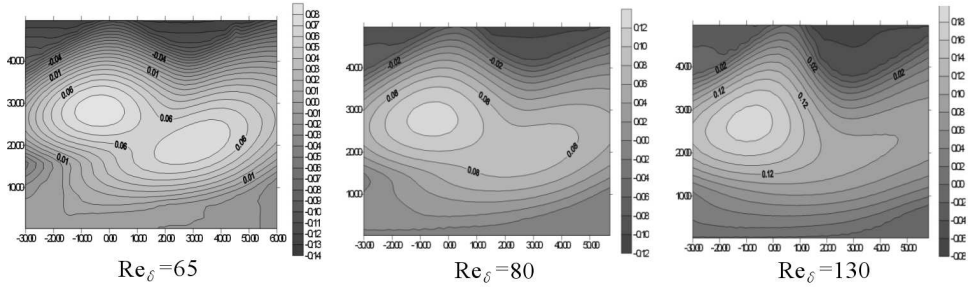

Fig. 2. Iso-lines of $\omega_i = $ const in the stationary disk boundary layer and at different local Reynolds numbers, in the plane of the wave-angle and wave-number (ε, k) (Tuliszka-Sznitko and Soong, 2000; Tuliszka-Sznitko et al., 2002)

In order to analyze the effect of thermal conditions we have extended our investigations (Tuliszka-Sznitko and Soong, 2000) to the non-isothermal class of flow. Calculations have been performed for different thermal Rossby numbers $B = \overline{\beta}(T_2^* - T_1^*)$; however, for validity of the Boussinesq approximation, the values of B have been limited to the range $|B| \leqslant 0.1$. From the definition of the thermal Rossby number, the positive and negative values of B stand for $T_2^* > T_1^*$ (hotter stator) and $T_2^* < T_1^*$ (hotter rotor), respectively. When the stator is cooled $(B < 0)$, buoyancy enhances in the rotor-stator cavity, producing a secondary flow which develops in opposite direction to the basic flow. On the contrary, when the rotor is cooled $(B > 0)$, the buoyancy driven secondary flow enforces the basic rotation driven flow. For $B > 0$, the fluid near the rotating disk is cooler than the fluid near the stationary disk. We have found that cooling of the stationary disk $B < 0$, stabilizes the flow with respect to both the type I and type II instabilities (Fig. 3a) by increasing the critical Reynolds numbers.

We use the Briggs (1964) criterion with a fixed wave number in the spanwise direction β to determine the region of absolute instability (Tuliszka-Sznitko et al., 2002). We have found that almost the entire layer on the stationary disk is absolutely unstable. The critical Reynolds number of the absolutely unstable flow has been found at $\mathrm{Re}_{\delta ca} = 48.5$. On the rotating disk, the critical Reynolds number of the absolutely unstable flow was determined at $\mathrm{Re}_{\delta ca} = 562$. In the next step, we extend our absolute/convective calculations to the non-isothermal class of flow (Tuliszka-Sznitko and Soong, 2000; Tuliszka-Sznitko et al., 2002). Fig.3b shows the neutral curves of absolutely unstable flow obtained for the stationary disk boundary layer and for different thermal Rossby

numbers (solid line). Fig. 3b presents also the second families of branch points
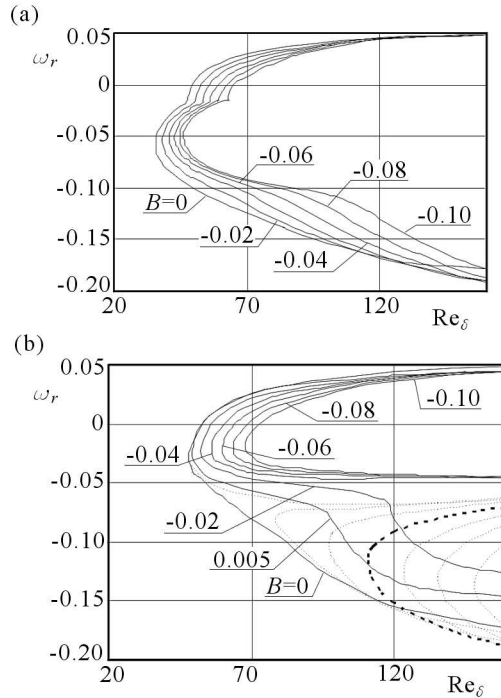(dashed line).

Fig. 3. Comparison of the neutral curves $\omega_r = f(\mathrm{Re}_\delta)$ in the stationary disk
boundary layer obtained at different thermal Rossby number B; (a) convectively
unstable areas, (b) absolutely unstable areas (dashed lines indicate second family)
(Tuliszka-Sznitko and Soong, 2000; Tuliszka-Sznitko *et al.*, 2002)

5.   DNS and LES results

5.1.   Cylindrical cavity

In this Section we will analyze shortly the results obtained using the DNS
method for cylindrical rotor/stator cavity of aspect ratio $L = 5$, with outer
cylinder attached to the stator (Serre *et al.*, 2004). The basic state consists of
two disjoint boundary layers on each disk and of a central inviscid core flow.
The fluid is pumped radially outwards, along the rotating disk (the upper
one) and radially inwards, along the stator. In order to obtain an insight into
the laminar-turbulent transition process in the rotor/stator flow, numerical
simulations have been performed for the Reynolds number close to the critical

Reynolds number of transition to unsteadiness. We gradually increased the Reynolds number and over a certain Re_R, and we have observed 2D cylindrical vortices propagating towards the axis of cavity in the stator's boundary layer. Cylindrical vortices are interpreted as the type II instability. Above a second critical Reynolds number, 3D spiral structures appeared (interpreted as type I instability) in the area near the outer end-wall. Spiral vortices propagate towards the outer cylinder i.e. in opposite direction to the direction of the basic state. This behavior could suggest (in accordance with the LSA results) that the area of dominance of type I in the stator boundary layer may be absolutely unstable. Exemplary structures obtained at $Re_R = 13200$ at the transient times $t = 60$ and $t = 320$ are presented in Fig. 4. This procedure was repeated for the flow additionally disturbed by superimposing on the initial condition at every consecutive Re_R, the 3D perturbation function of the general form $\eta \sin(p\varphi)$, where p is an arbitrary number corresponding to an azimuthal wavelength and η is the amplitude growth rate. Calculations have been performed for $\eta = 0\text{-}3.5$ and for $p = 2\pi/4$. We have found that for $\eta = 0$ the critical Reynolds number of transition to unsteadiness equals 12300. The amplitudes of disturbances in the stationary disk layer are much larger than the corresponding amplitudes in the rotating disk's boundary layer. This result is in good agreement with the similarity solution presented in the previous section. From the time history of the axial component of velocity in the stationary disk boundary layer (Fig. 5), we can see that disturbances are first damped and the flow reaches a steady state. Then we observe the beginning of the exponential growth of disturbances. Finally, these oscillations reach an asymptotic finite-amplitude periodic state with a constant angular frequency $\sigma = \omega^* Re_\delta \approx 1.1$.
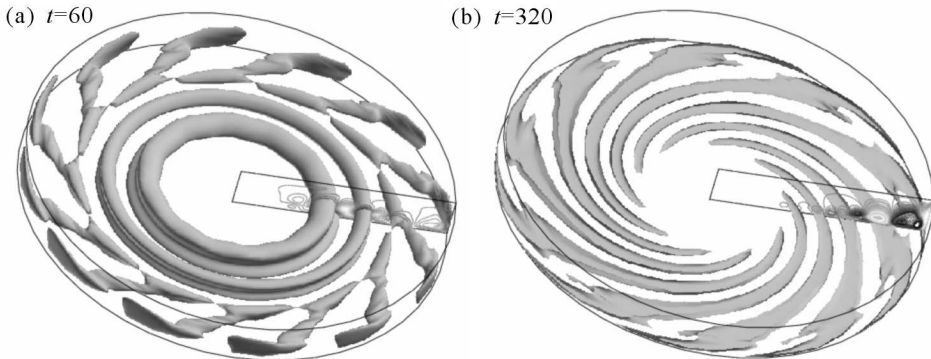
(a) t=60 (b) t=320

Fig. 4. Iso-surface of fluctuations of the axial component of velocity at $Re_R = 13200$, $\eta = 0$; (a) coexistence of annular and spiral structures related to Bödewadt layer instability during the transient time $t = 60$, (b) final state showing only 12 spiral arms (Serre *et al.*, 2004)
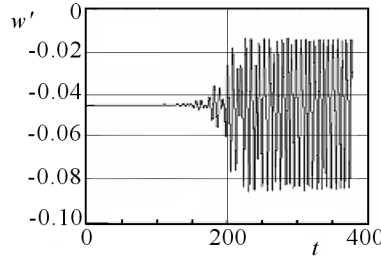
Fig. 5. Time histories of the axial component of velocity in the stationary disk
boundary layer; $\mathrm{Re}_R = 13200$, $\eta = 0$ (Serre *et al.*, 2004)

5.2. Annular cavity

In our investigations we performed computations for the annular cavities
with co- and counter-rotating disks of different aspect ratios L and different
curvature parameters R_m (Tuliszka-Sznitko and Zieliński, 2006a,b). However
in this section we have restricted our analysis to the results obtained for $L = 9$
and $R_m = 1.5$ and 3.0.

5.2.1. Rotor/stator cavity

We first focused on the steady axisymmetric basic state of the rotor/stator
case. Fig. 6 shows the velocity field in the meridional section $(r^*/h, z^*/h, 0)$
obtained for the rotor/stator case ($s = 0$, $\mathrm{Re}_R = 70000$, $B = 0$, the outer end-
wall attached to the rotor and inner end-wall attached to the stator). From
Fig. 6 we can see that the flow consists of two disjoint boundary layers on each
disk and of a central core flow. For arbitrary chosen positive value of s and
very small negative value, the meridional structure is similar to that obtained
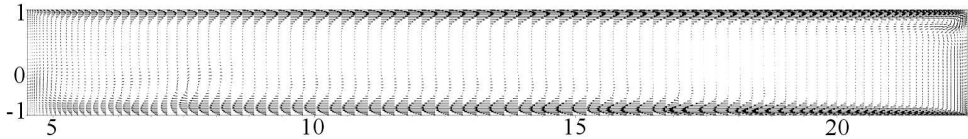for the rotor/stator case.

Fig. 6. Flow in the meridional section, rotor/stator cavity, $B = 0$, $L = 9$, $R_m = 1.5$,
$\mathrm{Re}_R = 70000$ (Tuliszka-Sznitko and Zieliński, 2006a,b)

In the annular cavity we observed the same instability structures as in the
cylindrical cavity. In stationary disk's boundary layer we observed two types
of vortices: 2D cylindrical vortices interpreted as type II instability and 3D
spiral vortices interpreted as type I instability. Fig. 7a shows the iso-lines of
the azimuthal velocity component disturbances, in azimuthal section $(r^*/h,$
$z^*/h = -0.95, \varphi)$ obtained for $L = 9$, $R_m = 1.5$, $\mathrm{Re}_R = 36000$ and for outer

end-wall attached to the stator and the inner one attached to the rotor. For this configuration in our DNS computations we observed 3 cylindrical vortices and 23 3D spiral vortices. The iso-lines of the axial velocity component disturbances in the meridional section $(r^*/h, z^*/h, \varphi = 0)$ are shown in Fig. 7c. The critical Reynolds number of transition to unsteadiness was estimated at $\mathrm{Re}_R = 34000$. Our results were compared with the experimental results obtained by Schouveiler *et al.* (1999, 2001) for the cavity of aspect ratio $L = 8.75$, $R_m = 1$, $\mathrm{Re}_R = 20900$ (the same outer end-wall condition). Schouveiler (1999, 2001) observed also 3 cylindrical vortices and 18 spiral vortices (Fig. 7b). Simlar computations, have been performed for the outer cylinder attached to the rotor and the inner one attached to the stator. For this configuration the critical Reynolds number of transition to unsteadiness equaled ~ 70000 and we observed 36 spiral vortices in the stationary disk boundary layer (Fig. 7d and Fig. 7f). These results were compared to the results obtained by Gauthier *et al.* (2002) for $L = 20.9$, $R_m = 1$ and for the outer cylinder attached to the rotor (Fig. 7e). We can see that for the considered cavity ($L = 9$, $R_m = 1.5$), the end-wall conditions have significant influence on the critical parameters. However, this influence is expected to be negligible in the limit of a large aspect ratio L.

Due to the CPU time requirements, DNS computations are limited to flows of low or moderate Reynolds numbers. For higher Reynolds numbers, the computations were performed using LES method. Fig. 8 shows the iso-lines of axial velocity component disturbances in the meridional section $(r^*/h, z^*/h, 0)$ obtained for the rotor/stator case and for $\mathrm{Re}_R = 36000$, 50000 and 75000 ($s = 0$, $L = 9$, $R_m = 1.5$, $B = 0$, the outer end-wall attached to the stator and the inner end-wall attached to the rotor). For $\mathrm{Re}_R = 50000$ and 75000 the results were obtained using LES method. The iso-lines of azimuthal velocity component disturbances in the azimuthal section obtained for $\mathrm{Re}_R = 75000$ are presented in Fig. 9. We can see that for $\mathrm{Re}_R = 75000$, the flow is at the last stage of the transition process.

5.2.2. *Rotor/rotor cavity*

In this section we consider the instability patterns of the flow between two counter-rotating disks and two cylinders. In the counter-rotating case, the centrifugal flow induced by the faster disk (upper one) recirculates along the slower rotating disk (lower one) towards the inner end-wall. This inward flow meets the outward radial flow induced by the slower rotating disk, leading to a stagnation area where the radial component of the velocity vanishes. In our computations we increased slowly the rotation of the upper disk $\mathrm{Re}_{R\,upper}$ from 6000 to 60000, with a fixed value of the bottom one $\mathrm{Re}_{R\,lower} = 3000$. The exemplary results are presented in Fig. 10. We can see that with incre-
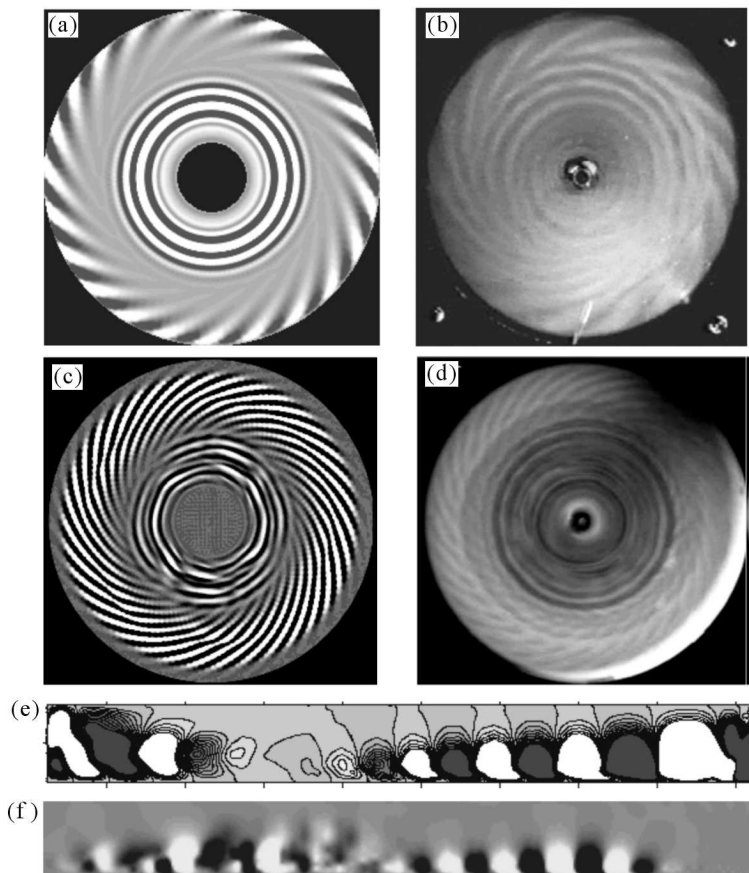
Fig. 7. (a) The iso-lines of azimuthal velocity component disturbances in the azimuthal section, $L = 9$, $R_m = 1.5$, $\mathrm{Re}_R = 36000$, the outer end-wall attached to the stator, (b) Schouveiler *et al.* (2001), experimental result, $R_m = 1$, $L = 8.75$, (c) the iso-lines of azimuthal velocity component disturbances in the azimuthal section, $z = -0.95$, $L = 9$, $R_m = 1.5$, $\mathrm{Re}_R = 75000$, the outer end-wall attached to the rotor, (d) Gauthier *et al.* (2002) experimental result, $R_m = 1$, $L = 20.9$, (e) the iso-lines of axial velocity component disturbances in the meridional section, $L = 9$, $R_m = 1.5$, $\mathrm{Re}_R = 36000$, (f) the iso-lines of axial velocity component disturbances in the meridional section, $L = 9$, $R_m = 1.5$, $\mathrm{Re}_R = 75000$ (Tuliszka-Sznitko and Zieliński, 2006a,b)

asing $\mathrm{Re}_{R\,upper}$ (with decreasing $|s|$), the stagnation circle moves from the outer cylinder toward the inner one. In Figs. 10a,b for $\mathrm{Re}_{R\,upper} = 6000$ and 20000 we can see that the boundary layers on the disks are separated by the shear layer. This free shear layer, which separates two regions of opposite angular rotations, breaks the azimuthal symmetry of the flow. The instability structures of free shear layer are observed for much lower Reynolds numbers
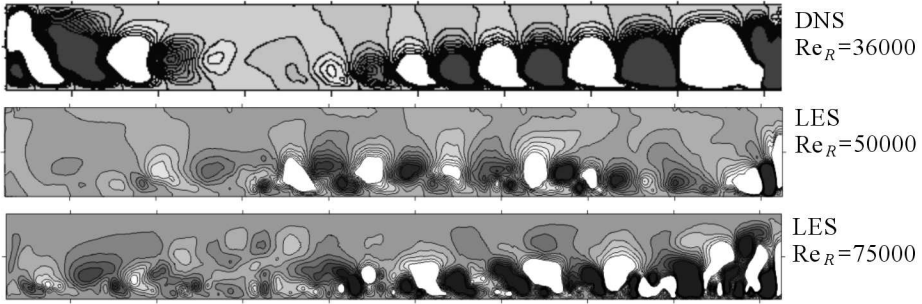
Fig. 8. The iso-lines of azimuthal velocity component disturbances in the meridional section, $L = 9$, $R_m = 1.5$, $\mathrm{Re}_R = 36000, 50000, 75000$
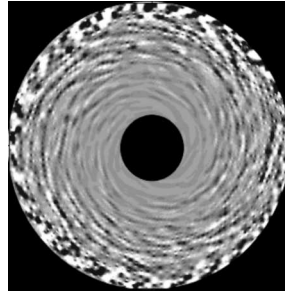

Fig. 9. The iso-lines of azimuthal velocity component disturbances in the azimuthal section $z = -0.95$, obtained for $\mathrm{Re}_R = 75000$, $L = 9$, $R_m = 1.5$, $s = 0$, $B = 0$
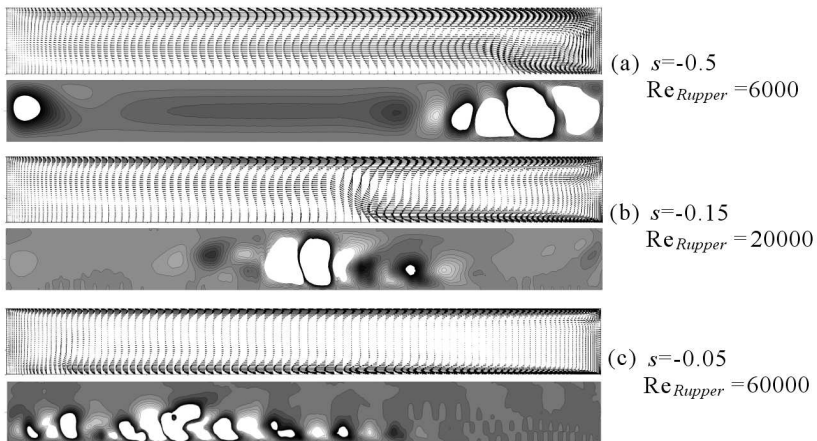

Fig. 10. The flow and the corresponding iso-lines of axial velocity component disturbances in meridional section obtained for $\mathrm{Re}_{R\,lower} = 3000$, and for $\mathrm{Re}_{R\,upper} = 6000, 20000, 600000$, $L = 9$, $R_m = 1.5$ (Tuliszka-Sznitko and Zieliński, 2006a)

than the critical Reynolds numbers of type II and I instability in the rotating disks boundary layers. For some combination of parameters ($\text{Re}_{R\,lower}$, $\text{Re}_{R\,upper}$), interaction between the Ekman layer and the still existing shear layer results in negative spirals. The negative spiral vortices obtained for $\text{Re}_{R\,upper} = 60000$ are presented in Fig. 11a (azimuthal section). In Fig. 11b the experimental results obtained by Gauthier for $L = 20.9$ are shown. We can see very good agreement between our numerical results and the experimental results obtained by Gauthier *et al.* (2002), Fig. 11.
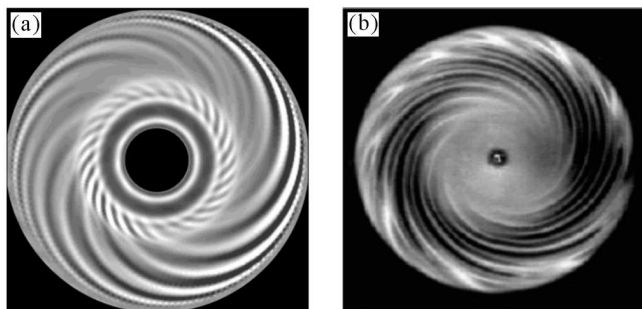

Fig. 11. (a) The iso-lines of azimutal velicity component disturbances in azimuthal section obtained for: $\text{Re}_{R\,lower} = 3000$ and for $\text{Re}_{R\,upper} = 60000$, $z = 0.844$ (Tuliszka-Sznitko and Zieliński, 2006a), (b) experimental results of Gauthier *et al.* (2002)

5.3. Rotor/rotor configuration with throughflow

In this section we analyze the flow in a rotor/rotor cavity of $s = 1$ (both disks rotate in the same direction with the same rotational speed) with throughflow. We consider a radial outflow of fluid from a source at the inner cylinder to a sink at the outer cylinder. Computations with throughflow require changes in the boundary conditions at the cylinders (in comparison with cases of impermeable cylinders considered in previous chapters). For the inner and outer cylinders we have the following boundary conditions:
— for $r = -1.0$

$$u = \frac{C_w L (R_m + 1)^2}{4\pi \text{Re}_R (R_m + r)} \qquad v = w = 0$$

— for $r = 1.0$

$$u = \frac{C_w L (R_m + 1)^2}{4\pi \text{Re}_R (R_m + r)} \qquad v = w = 0$$

where $C_w = \dot{V}^*/R_1^* \nu^*$ is a dimensionless volume flow rate. In our computations we proceeded as follows: with the fixed Reynolds number we slowly increased

C_w and the result obtained for smaller C_w was used as the initial condition for higher C_w. The basic state is steady and axisymmetric. The exemplary meridional velocity field obtained for $\mathrm{Re}_R = 200000$ and $C_w = 700$ ($L = 9$, $R_m = 3$) is displayed in Fig. 12a. We can see that for isothermal radial outflow from a uniform source at R_0^* to a uniform sink at R_1^*, the meridional flow can be divided into three regions: an inner source, separated Ekman layers on each disk and an outer sink layer. In our computations, in order to accelerate the transition to unsteadiness, the axisymmetric basic flow was perturbed near the inner cylinder by superimposing a disturbance of the following form: $\eta \sin(p\varphi)$ (as in Section 5.1). Results presented in Fig. 12b were obtained for $p = 1/4$ and $\eta = 3.4$. We can see that the most unstable regions are sink and source areas. Four pairs of 2D counter-rotating rolls in both the Ekman layers are visible. Superimposed disturbance near the inner end-wall produced the rise of weak 8 spiral vortices in this area.
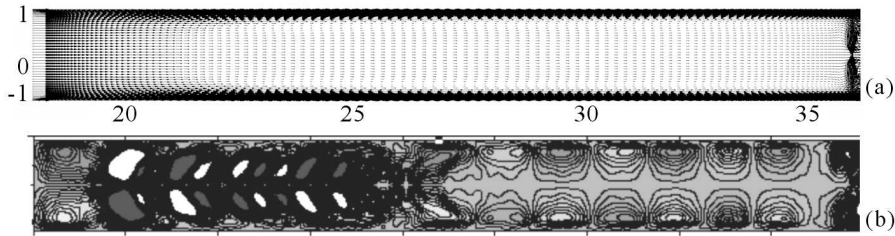

Fig. 12. The mean flow (a) and the iso-lines of axial velocity component disturbances in meridional section obtained for $\mathrm{Re}_R = 200000$, $C_w = 700$, $B = 0$, $L = 9$, $R_m = 3$ (Tuliszka-Sznitko and Zieliński, 2006a)

5.4. Non-isothermal flow in annular cavity

The heat transfer in flow between two rotating disks is a problem of great importance to the gas-turbine air cooling designer. In this chapter we present our exemplary results obtained for the non-isothermal flow to estimate the influence of the thermal Rossby number on the basic state, distribution of the local Nusselt numbers and on the instability structures.

5.4.1. Rotor/stator configuration

The influence of the thermal Rossby number on the basic state is small. However, we have found a significant influence of B on the critical Reynolds number of transition to unsteadiness. As we expected, the critical Reynolds number of transition to unsteadiness in the stationary disk's boundary layer increases with decreasing B. The instability structures obtained for the non-isothermal flow are roughly the same as those for the incompressible cases. In

the rotor/stator cases we observed 2D cylindrical vortices for the lower Reynolds number and positive 3D spiral vortices for the higher Reynolds number, however we have found that the number of spiral vortices decreases with increasing B. To verify our non-isothermal results we compared distribution of the local Nusselt numbers on the rotating disk ($L = 9$, $R_m = 1.5$, outer end wall attached to the stator and inner one to the rotor) with the experimental data of Mochizuki and Yang Wen-Jei (1986) and with the results obtained for a single heated rotating disk using the similarity analysis. Agreement of the results is good. Exemplary distributions of Nu along the radius r^*/h obtained from DNS computations and from the similarity equations for the single heated rotating disk for $B = -0.1$, $\mathrm{Re}_R = 25000$, 35000, 47000 are presented in Fig. 13. The local Nusselt number is calculated from the following equation

$$Nu = \frac{\alpha^* r^*}{\lambda^*} = -\left(\frac{\partial \Theta}{\partial z}\right)_w \frac{r^*}{h} \frac{1}{\Theta_w - \Theta_c} \tag{5.1}$$

where Θ_C is the dimensionless temperature of inviscid core, λ^* is the coefficient of thermal conductivity, α^* is the coefficient of heat transfer and index w a indicates parameter at the wall. In Fig. 13 the areas near the end-walls were cut off because of difficulties with definition of temperature Θ_C near the cylinders. From Fig. 13 we can see that the DNS and the similarity solutions (straight broken lines in Fig. 13) coincide well along a large part of the rotor.
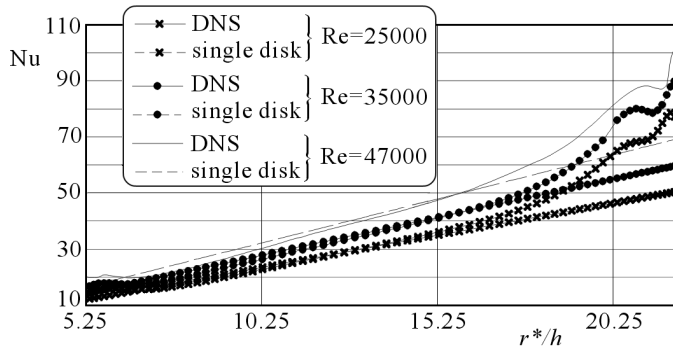

Fig. 13. The exemplary distributions of the local Nusselt number on the rotor obtained for $B = -0.1$, $\mathrm{Re}_R = 25000$, 35000, 47000 (Tuliszka-Sznitko and Zieliński, 2006a)

5.4.2. Rotor/rotor configuration with throughflow

The most interesting from the point of view of turbomachinery air cooling devices are examples with the superimposed radial outflow. In Fig. 14 the isolines of temperature and disturbances of the axial velocity component obtained for $L = 9$, $R_m = 3$, $\mathrm{Re}_R = 200000$, $B = 0.1$, $t = 16$ and C_w from 300 to 700

are displayed. Both disks rotate in the same direction with the same angular speed and on both disks $\Theta = 1$. The boundary conditions at the inner and outer cylinders are as follows:

— for $r = -1.0$

$$u = \frac{C_w L (R_m + 1)^2}{4\pi \mathrm{Re}_R (R_m + r)} \qquad v = w = 0 \qquad \Theta = 0$$

— for $r = 1.0$

$$u = \frac{C_w L (R_m + 1)^2}{4\pi \mathrm{Re}_R (R_m + r)} \qquad v = w = 0 \qquad \Theta = 1$$

Figures 14 show the effectiveness of radial cooling; the areas dominated by coming cooling air are laminar for all considered mass flow rates.
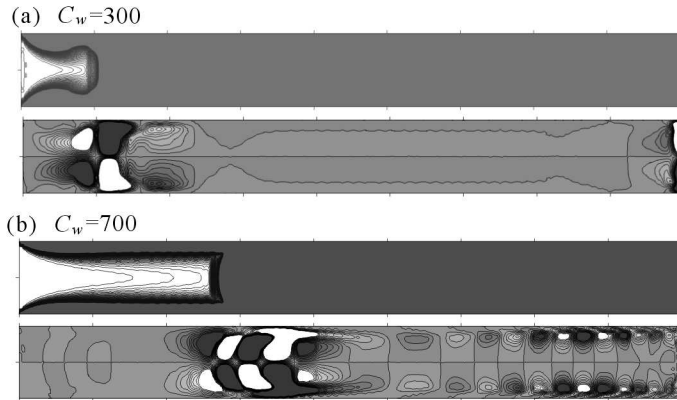
(a) C_w=300

(b) C_w=700

Fig. 14. The iso-lines of temperature and disturbances of the axial velocity component obtained for $L = 9$, $R_m = 3$, $\mathrm{Re}_R = 200000$, $B = 0.1$, $t = 16$ and $C_w = 300$ and 700

6. Conclusions

In the present paper results of numerical simulation of the transitional flow with heat transfer in a rotating cavity were reviewed. The isothermal and non-isothermal 3D fluid flows between co- and counter-rotating disks enclosed by two rotating cylinders, were investigated. Computations have been performed using the DNS, LES and LSA methods. Special attention has been paid to the basic laminar flow in order to obtain more insight into the onset of the different instability patterns and their regions of existence. Three different patterns

have been found: axisymmetrically propagating vortices interpreted as type II instability, positive spiral vortices interpreted as type I instability and negative spirals. The first two vortices, i.e. cylindrical vortices and positive spirals were present in all the considered configurations; cylindrical and annular cavities of the different aspect ratios and curvature parameters. Negative spirals, which exist in the counter-rotating configurations, differ significantly from the 2D and positive 3D vortices. First of all, the negative spirals rotate around the central axis and the mechanism is not of a cross-flow type; it is probably the result of interaction between free shear layer and the Ekman layer. We have found that the negative spirals can co-exist with the positive vortices. These results were discussed using the experimental results of Gauthier *et al.* (2002). Comparison shows a good agreement. Our LSA computations also turned out to be very useful in interpretation of 2D and positive 3D vortices in terms of the type II and type I instability. Additionally, the LSA allowed us to identify the areas of absolutely unstable flow.

The configurations which are most interesting from the point of view of possible applications are those with the superimposed flow (flow with the source and sink). For the incompressible configuration we have found similar instability structures as those in paper by Serre *et al.* (2001b). We extended these computations to the non-isothermal cases.

Our non-isothermal results showed that influence of the thermal Rossby number on instability structure is not large, however we have found significant influence B on the critical Reynolds number of transition to unsteadiness. Distributions of the local Nusselt numbers along the radius of the disk show a good agreement with the experimental data of Mochizuki and Yang Wen-Jei (1986) and with theoretical solutions. Computations showed effectiveness of the radial cooling.

References

1. Bohn D., Emunds R., Gorzelitz V., Krliger U., 1994, Experimental and theoretical investigations of heat transfer in closed gas filled annuli II, *ASME Int. Gas. Turbine and Aeroengine Cong.*, The Hague, Paper 94-GT-175

2. Briggs R., 1964, *Electron-Stream Interaction with Plasmas*, MIT Press

3. Chew J., Owen J., Pincombe J., 1984, Numerical prediction for laminar source-sink flow in a rotating cylindrical cavity, *J. Fluid Mech.*, **143**, 451-466

4. DIJKSTRA D., AND VAN HEIJST G., 1983, The flow between two finite rotating discs enclosed by a cylinder, *J. Fluid Mech.*, **128**, 123, 123-154

5. GAUTHIER G., GONDRET P., MOISY F., RABAUT M., 2002, Instabilities in the flow between co- and counter-rotating disks, *J. Fluid Mech.*, **473**, 1-21

6. GERMANO M., PIOMELLI U., MOIN P., CABOT W., 1991, A dynamic sub-grid eddy viscosity model, *Phys. of Fluids A*, **3**, 1760-1765

7. ITOH M., 1991, On the instability of the flow between coaxial rotating disks, In: *Boundary Layer Stability and Transition to Turbulence*, ASME FED 114, 83-89

8. LINGWOOD R., 1997, Absolute instabilities of the Ekman layer and related rotating flows, *J. Fluid. Mech.*, **331**, 405-428

9. MENEVEAU C., LUND T., CABOT W., 1996, A Lagrangian dynamic subgrid-scale model of turbulence, *J. Fluid Mech.*, **319**, 353-385

10. MOCHIZUKI S., YANG WEN-JEI, 1986, Flow friction on co-rotating parallel-disk assemblies with forced through-flow, *Experiments in Fluids*, **4**, 56-60

11. MOISY F., DOARE O., PASUTTO T., DAUBE O., RABAUD M., 2004, Experimental and numerical study of the shear layer instability between two counter-rotating disks, *J. Fluid Mech.*, **507**, 175-203

12. OWEN J., ROGERS R., 1995, *Heat Transfer in Rotating Disc Systems, Vol. 2: Rotating Cavity*, W.D. Morris (Edit.), Wiley

13. SCHOUVEILER L., LE GAL P., CHAUVE P., TAKEDA Y., 1999, Spiral and circular waves in the flow between a rotating and a stationary disc, *Experiments in Fluids*, **26**, 179

14. SCHOUVEILER L., LE GAL P., CHAUVE P., 2001, Instabilities of the flow between a rotating and stationary disk, *J. Fluid Mech.*, **443**, 329-350

15. SERRE E., CRESPO DEL ARCO E., BONTOUX J., 2001a, Annular and spiral patters in flow between rotating and stationary disks, *J. Fluid. Mech.*, **434**, 65, 65-100

16. SERRE E., HUGUES S., CRESPO DEL ARCO E., RANDRIAMAMPIANINA A., BONTOUX P., 2001b, Axisymmetric and three-dimensional instability in an Ekman boundary layer flow, *Int. J. Heat Fluid Flow*, **22**, 82-93

17. SERRE E., TULISZKA-SZNITKO E., BONTOUX P., 2004, Coupled numerical and theoretical study of the flow transition between a rotating and stationary disk, *Phys. of Fluids*, **16**, 3

18. TULISZKA-SZNITKO E., SOONG C.Y., 2000, Instability of non-isothermal flow between coaxial rotating disks, *Proceedings of European Congress on Computational Methods in Applied Sciences and Engineering*, Barcelona

19. TULISZKA-SZNITKO E., SERRE E., BONTOUX P., 2002, On the nature of the boundary layers instabilities in a flow between a rotating and a stationary disc, *C.R. Mecanique*, **30**, 90-99

20. Tuliszka-Sznitko E., Zieliński A., 2006a, Instability of the isothermal and not-isothermal flow in rotating cavity of aspect ratio 9, *Proceedings of ISTP17*, Japan

21. Tuliszka-Sznitko E., Zieliński A., 2006b, Numerical investigation of the transitional flow in co- and counter-rotating annular cavity, *Journal of Theoretical and Applied Mechanics*, **44**, 2, 405-421

Niestabilność przepływów w wirujących przestrzeniach

Streszczenie

W pracy dokonano analizy wyników dotychczasowych prac własnych nad statecznością przepływów w wirujących przestrzeniach. Badania te prowadzono metodą liniową, metodą DNS i LES. Do trójwymiarowych obliczeń numerycznych zastosowano metodę spektralnej kolokacji bazującą na szeregach Czebyszewa i szeregu Fouriera. Do metody LES zastosowano metodę Lagrangea zaproponowaną przez Meneveau. Głównym celem było zbadanie struktur niestabilnościowych występujących w wirujących przestrzeniach. Wyniki te porównano z wynikami prac eksperymentalnych innych autorów. Badano wpływ termicznej liczby Rossbiego na rozkłady liczb Nusselta wzdłuż promienia tarcz oraz efektywność chłodzenia promieniowego tarcz za pomocą napływającego chłodnego czynnika.